

# High Energy Density Micro-Supercapacitor Based on a Three-Dimensional Bicontinuous Porous Carbon with Interconnected Hierarchical Pores

Xinyu Ma,<sup>†</sup> Xufeng Hong,<sup>†</sup> Liang He,<sup>\*,†,‡</sup> Lin Xu,<sup>†</sup> Yanjia Zhang,<sup>†</sup> Zhe Zhu,<sup>†</sup> Xuelei Pan,<sup>†</sup> Jiexin Zhu,<sup>†</sup> and Liqiang Mai<sup>\*,†</sup>

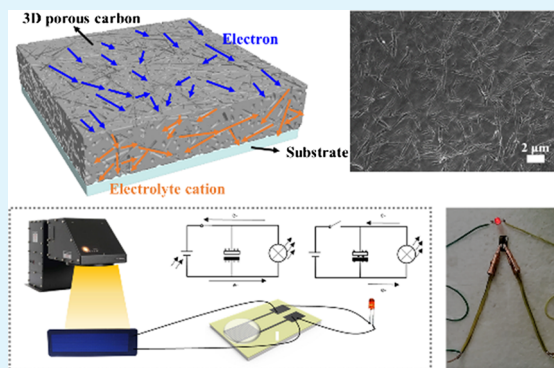
<sup>†</sup>State Key Laboratory of Advanced Technology for Materials Synthesis and Processing, Wuhan University of Technology, Wuhan 430070, P. R. China

<sup>‡</sup>Department of Materials Science and NanoEngineering, Rice University, Houston, Texas 77005, United States

## Supporting Information

**ABSTRACT:** On-chip micro-supercapacitors (MSCs) have attracted great attention recently. However, the performance of MSCs is usually unsatisfactory because of the unreasonable pore structure. The construction of a three-dimensional (3D) interconnected porous carbon-based MSC by controllable activation is proposed. The porous monolithic carbon microelectrode activated by ZnO nanowires provides electron/ion bicontinuous conduction path. The fabricated MSC with this microelectrode rendered a high areal specific capacitance of 10.01 mF cm<sup>-2</sup>, 6 times higher than that of pure pyrolyzed carbon-based MSC, 1.6–5 times higher than that of the MSC with porous carbon activated by ZnO nanoparticles because of its cross-linking macropore–mesopore–micropore structure and considerable areal atomic ratio. The optimization mechanism of the hierarchical channel pore for the electrochemical performance of MSCs is investigated in detail. Four kinds of electrolytes, including H<sub>2</sub>SO<sub>4</sub>, redox additive KI/H<sub>2</sub>SO<sub>4</sub>, LiCl, and LiTFSi, are employed for constructing MSCs. The voltage window of water in a salt electrolyte assembled LiTFSi-MSC is expanded to 2.5 V. The energy density of LiTFSi-MSC is 6 times higher than that of H<sub>2</sub>SO<sub>4</sub>-MSC, which can drive light-emitting diodes without serial or parallel connection. This high-performance 3D interconnected porous carbon-based MSC shows a great potential in applications for large-scale integration of micro-/nanodevices.

**KEYWORDS:** micro-supercapacitor, bicontinuous, porous carbon, channel pore, hierarchical, water-in-salt electrolyte



## INTRODUCTION

The large-scale integration and miniaturization of intelligent electronic devices have high requirements for the performance of their energy supply systems.<sup>1–4</sup> Micro-supercapacitors (MSCs) with higher charge–discharge rate, ultralong cyclic lifetime, and considerable energy density have attracted more attention than microbatteries in the past decade.<sup>4,5</sup> Unlike bulk supercapacitors, MSC is more focused on the compatibility and rationality of manufacturing process and controllable preparation of microelectrodes.<sup>6–9</sup> For the microfabrication process of MSCs (micron level), plasma etching,<sup>6</sup> physical vapor deposition,<sup>12</sup> electrochemical deposition,<sup>13,14</sup> and other processes<sup>5,15</sup> have been extensively studied. The coordination of their fabrication process and optimization of the electrode structure as a considerable strategy have been widely proposed, aiming to predigest the fabrication process with the substantive increase of energy storage performance of MSCs.<sup>11,16,17</sup>

For the two types of energy storage mechanisms, electric double-layer capacitor (EDLC) is based on physical adsorption of ions over interfaces between the electrode and electrolyte,

whereas the pseudocapacitor stores energy by the redox action of the electrode with ions in the electrolyte.<sup>19–21</sup> In the view of previous work, the supercapacitors with inert electrodes such as pyrolyzed carbon<sup>22–24</sup> and graphene<sup>26</sup> have definitely unlimited lifetime which exceeds that of pseudocapacitors. With a view to the applications of MSCs such as home automation, transport surveillance, and industrial processes' tracking, the MSCs require higher cycling life because of the repeated charge and discharge and long working life.<sup>9,27,28</sup> Thus, the advantages of inert electrodes represented by carbonaceous materials are more obvious than those of pseudocapacitive materials such as MnO<sub>2</sub> and polypyrrole (PPy).<sup>29–31</sup> As one of carbonaceous materials, pyrolyzed carbon has been employed as the commercial electrode of SCs; however, there are some distinctive shortages, limiting the increase of their energy density such as clog of mesopores by

Received: October 28, 2018

Accepted: December 6, 2018

Published: December 6, 2018

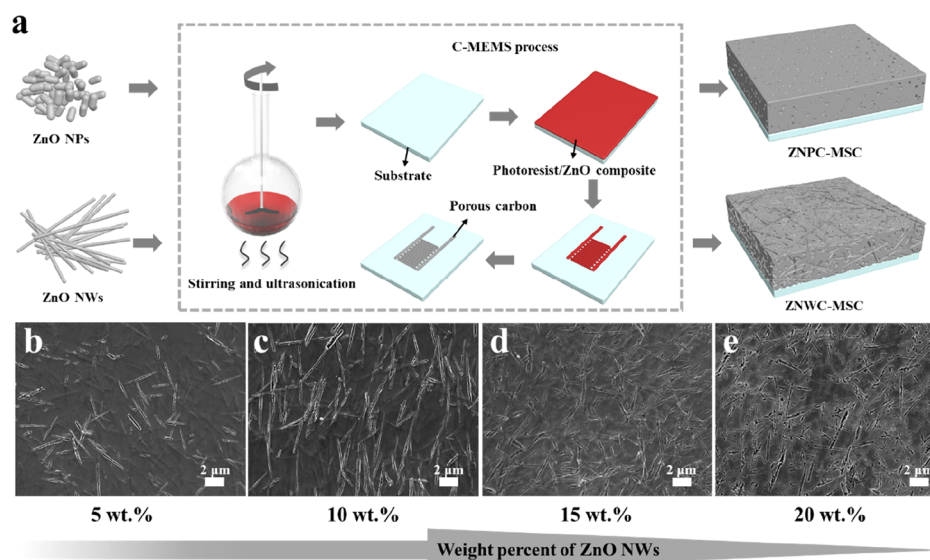


**Figure 1.** (a) Microfabrication process of ZNPC-MSC and ZNWC-MSC. After compositing PR1-9000A with ZnO NPs or ZnO NWs, the ZnO nanomaterial/photoresist composite was spin-coated on the wafer and then pyrolyzed after micropatterning by photolithography. (b–e) SEM images of pyrolyzed carbon microelectrodes activated by 5–20 wt % ZnO NWs.

binders and monotonous pore structures, decreasing the accessibility of the electrolyte to the distributed pore area of the material.<sup>33–35</sup> The distribution of Ohmic resistance associated with the electrolyte over the interface between the electrode and electrolyte determines the estimation of the effective pore volume.<sup>36</sup> Hence, the structure of the inert electrode should have a fundamental role associated with the energy density of MSCs by broadening the diffusion access of ions and improving the specific surface area (SSA).

In addition, the controllable modification of the porous structure of pyrolyzed carbon and the diversity of its molding process access the operability and application of MSCs.<sup>22</sup> A carbon-based microelectromechanical system (C-MEMS) performed as a typical microfabrication platform of micro-devices has attracted wide potential applications similar to MSCs with porous pyrolyzed carbon microelectrodes.<sup>39–42</sup> The pathway of constructing a three-dimensional (3D) carbon-based structure for increasing the SSA and infiltration property of the electrolyte is effectively scarce yet very difficult especially for the thin-film electrode of MSCs owing to the limitation of microfabrication and stability of the microelectrode. Thus, combining the simple but efficient microfabrication processes with universal constructing strategies of carbon-based 3D pores to enhance the performance of MSC is the biggest challenge.

Hence, we efficiently demonstrated a method for the combination of microfabrication with material optimization to enhance the performance of MSCs. The MSC is fabricated by C-MEMS technology, whose microelectrode is optimized by constructing a 3D pore structure via the activation of ZnO nanoparticles (ZnO NPs) and ZnO nanowires (ZnO NWs), respectively. Additionally, the performance-enhanced mechanism of 3D microelectrode-based MSCs activated by ZnO NPs and ZnO NWs is investigated clearly, which proves deeply the importance of the 3D pore structure and electron/ion bicontinuous conduction path especially for the thin-film electrode. Pyrolyzed carbon-based MSCs activated by ZnO NWs (the weight percent of ZnO in the photoresist/ZnO composite is 15%) rendered a high areal specific capacitance of 10.01 mF cm<sup>-2</sup> because of its high electrical conductivity and

cross-linked pore structure (i.e., 3D pore structure). Also, four types of electrolytes are employed to improve the energy density of MSCs via the increase of specific capacitance and voltage window. After comparison of the specific energy densities of MSCs, we have full confidence in the application of LiTFSi [lithium bis(trifluoromethane sulfonyl)imide] for MSCs because of the highest energy density of 4.9 μW h cm<sup>-2</sup>, which is 6 times that of H<sub>2</sub>SO<sub>4</sub>. The single MSC with the LiTFSi electrolyte is used to drive the light-emitting diode (LED, operating voltage > 1.8 V) because of its high energy density and voltage window of 2.5 V.

## RESULTS AND DISCUSSION

To obtain desirable ZnO NPs and ZnO NWs applied as hard templates, we choose the facile coprecipitation and hydrothermal methods to synthesize ZnO NPs and ZnO NWs, respectively (see details in the “Experimental Section in the Supporting Information”). As shown in Figure S1a (Supporting Information), the synthesized ZnO NPs with ~100 nm in diameter dispersed uniformly without obvious aggregation. The X-ray diffraction (XRD) pattern of ZnO NPs shows that all peaks can be well indexed to hexagonal zinc oxide (JCPDS card no. 01-079-0208, Figure S1c). The synthesized ZnO NWs with ~100 nm in diameter and 10 μm in length also belong to hexagonal zinc oxide (JCPDS card no. 01-079-2205, Figure S1d). As shown in Figure 1a, the PR1-9000A photoresist composited with uniformly dispersed ZnO NPs and ZnO NWs, respectively, is pyrolyzed to micropatterned porous carbon via the optimized C-MEMS microfabrication process. The optical graph of carbon-based MSCs activated by 15 wt % ZnO NWs (15 ZNWC-MSC, activated by 5, 10, and 20 wt % ZnO NWs, i.e., 5 ZNWC-MSC, 10 ZNWC-MSC, and 20 ZNWC-MSC, respectively) shows the MSC with high fabrication precision (Figure S2a).

The carbothermic reduction [C(s) + ZnO(s) → C'(s) + Zn(g) + CO(g)] leads to the sacrifice of pyrolyzed carbon.<sup>22</sup> The field emission scanning electron microscopy (SEM) images of carbon-based microelectrodes activated by ZnO NWs with stepped values of 5, 10, 15, and 20 wt %,

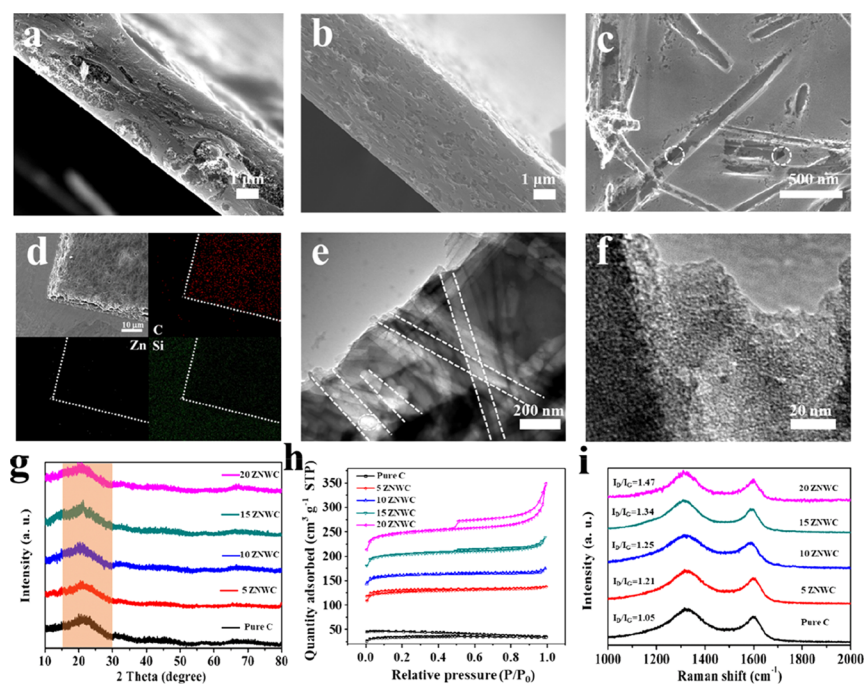


**Figure 2.** SEM images of carbon-based microelectrodes activated by (a) 15 wt % ZnO NPs and (b,c) 15 wt % ZnO NWs. (d) EDS elemental mapping, (e,f) TEM images of carbon-based microelectrodes activated by 15 wt % ZnO NWs. (g) XRD patterns, (h) BET adsorption–desorption curves, and (i) Raman spectra of carbon-based microelectrodes activated by 0, 5, 10, 15, and 20 wt % ZnO NWs.

respectively, are shown in Figure 1b–e. One-dimensional (1D) channel structure (about 100 nm in diameter) created by the reduction of ZnO and evaporation of Zn could be found easily. Besides, the amount of 1D pores obviously increases with the weight percent of ZnO NWs ranging from 5 to 20 wt %. Morphologies of carbon activated by ZnO NPs (ZNPC) are shown in Figure S3. The agglomerate of macropores (about 100 nm in diameter) could be observed because of the aggregation of ZnO NPs, which will relatively decrease the SSA of active carbon.

To evaluate the differentiated effect of carbon-based microelectrodes activated by ZnO NWs and ZnO NPs, the cross-sectional SEM images of carbon-based microelectrodes activated by 15 wt % ZnO NWs and ZnO NPs are shown in Figure 2a,b. The joint parts of channel pores are marked by white dashed circles as shown in Figure 2c. Some pores are connected and the 1D channels reunite to form a 3D pore structure (Figure 2b,c), different from the agglomerate of macropores activated by 15 wt % ZnO NPs (Figure 2a). The thickness of the 15 ZNWC microelectrode is 4.4 μm, which is similar to that of the pure pyrolyzed carbon microelectrode. As shown in Figure 2d, the energy-dispersive spectroscopic (EDS) elemental mapping images of the carbon-based microelectrode activated by 15 wt % ZnO NWs provide clear evidence of the absence of the Zn element and the existence of C, which correspond well with the result of its XRD pattern (Figure 2g). Also, transmission electron microscopy (TEM) image of the 15 ZNWC-MSC microelectrode exhibits a cross-linking pore with a diameter of 100 nm (Figure 2e). The mesopores are found on the tough wall of cross-linking macropores (Figure 2f). Furthermore, the carbonization and pyrolysis–reduction processes were conducted by thermogravimetric (TG) analysis and differential scanning calorimetry (DSC), respectively, as shown in Figure S4. The carbothermic reduction of ZnO and evaporation of Zn

occurred at ~400 and 900 °C, respectively. In the XRD patterns (Figures 2g and S5), the pyrolyzed carbon produced by the carbothermic reduction of ZnO nanomaterials displays a broad graphite stacking peak at  $2\theta = 21.3^\circ$ . The disappearance of ZnO diffraction peaks indicates the complete reduction of ZnO NWs and the evaporation of Zn, which is consistent with the result of EDS mapping (Figure 2d). The SSA and pore volume of pyrolyzed carbon activated by ZnO NWs and ZnO NPs with the increased content determined, respectively, by the Brunauer–Emmett–Teller (BET) method show the adjustable regularity (Figures 2h and S6 and Table S1).

After being activated by ZnO with the same weight percent, the pyrolyzed carbon activated by ZnO NWs reveals a relatively higher SSA than that of ZnO NPs because of more sufficient utilization of the 1D structure of ZnO NWs as the template agent (Table S1). As the proportion of ZnO increases, the mesoporosity with a diameter of 4 nm in the activated carbon (AC) also increases (Figure S6). The surface area of the pyrolyzed carbon activated by ZnO NWs is high because of the hierarchical pore. We conducted the Raman spectroscopy characterization to investigate the activation level. As shown in Figure 2i, the increase of  $I_D/I_G$  can be observed with the increase of ZnO NWs, demonstrating the increment of defects caused by activation with ZnO NWs and ZnO NPs of relatively high content (Figure S7). In general, ZnO is successfully used as a template to optimize the pore structure of pyrolyzed carbon. The amount of ZnO in a photoresist has a significant effect on its SSA but has no significant effect on the structure of mesopores. Different morphologies of ZnO as the template agent have a significant effect on the structure and SSA of the pyrolyzed carbon macroporous network.

The electrochemical performances of ZNWC-MSCs and ZNPC-MSCs with ZnO of the gradient content were examined by cyclic voltammetry (CV) and galvanostatic charge–discharge (GCD). The CV curves of C-MSC (i.e., MSC

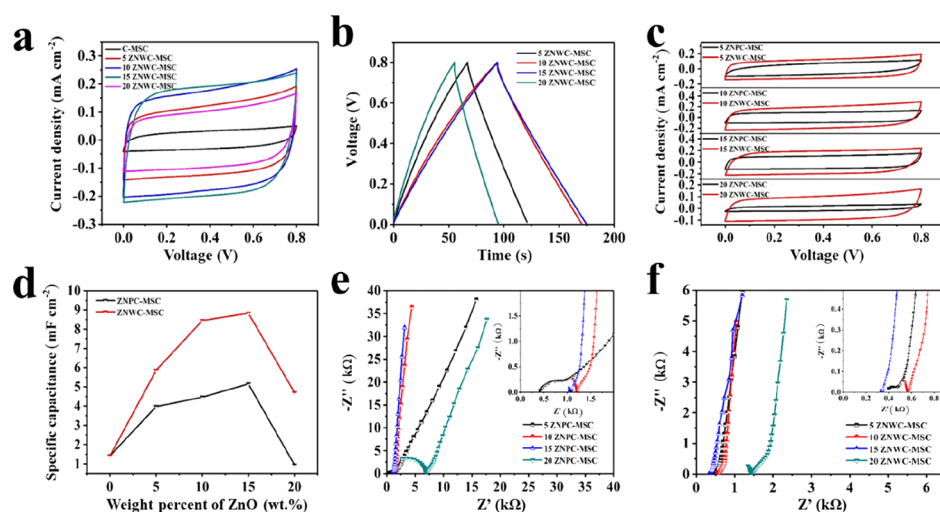


**Figure 3.** Electrochemical performances of carbon-based MSCs activated by ZnO NPs and ZnO NWs with the gradient content. (a) CV curves of pure C-MSC and 5–20 ZNWC-MSCs at the scan rate of  $20 \text{ mV s}^{-1}$  and (b) GCD curves of 5–20 ZNWC-MSCs at the current density of  $0.1 \text{ mA cm}^{-2}$ . (c) CV curves of carbon-based MSCs activated by ZnO NPs and ZnO NWs. (d) Specific capacitance curves (vs weight percent of ZnO) of carbon-based MSCs activated by ZnO NPs and ZnO NWs with the gradient content calculated by GCD curves at  $0.1 \text{ mA cm}^{-2}$ . EIS curves of (e) 5–20 ZNPC-MSCs and (f) 5–20 ZNWC-MSCs.

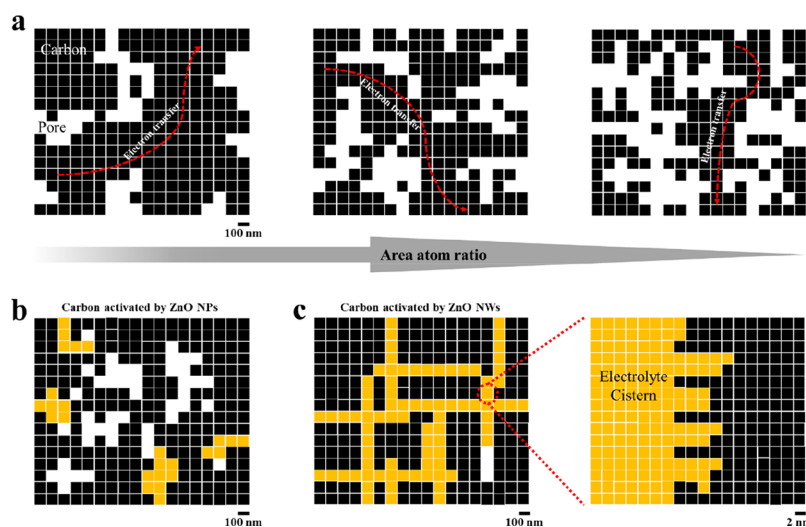


**Figure 4.** (a) Sketches of a two-dimensional cross section of the 3D pore structure are shown to visualize the concepts of the areal atom ratio. The electrical conductivity of carbon will decrease with the increase of the areal atom ratio. (b) Sketch of carbon activated by ZnO NPs with the infiltration of the electrolyte. (c) Sketch of carbon activated by ZnO NWs with the infiltration of the electrolyte, and the status of mesopores on the wall of pores formed by ZnO NWs.

based on pyrolyzed carbon without any activation with ZnO), 5, 10, 15, and 20 ZNWC-MSCs, respectively, show synchronously the quasi-rectangular shape, which is characteristic for ideal EDLC with little electrolyte diffusion limitation (Figure 3a). As shown in Figure 3b, the GCD curves of 5–20 ZNWC-MSCs show a symmetrical triangle with relatively unobvious IR drop ( $10\text{--}35 \text{ mV}$  at  $0.1 \text{ mA cm}^{-2}$ ) related to the electrical conductivity of microelectrodes that will be discussed below (Table S2). The similar results of ZNPC-MSC are also obtained (Figure S8a,b). To further investigate the effect of activation by ZnO with different morphologies, we compared the CV curves of pyrolyzed carbon-based MSCs activated by 5–20 wt % ZnO NWs and ZnO NPs, respectively. As shown in Figure 3c, the CV curve areas of ZNWC-MSCs are previously larger than those of ZNPC-MSCs with the different activated content values of ZnO. In order to

quantitatively compare the effect of these two activation modes on the capacitance of MSCs, we compared the specific capacitances of MSCs activated by ZnO NWs and ZnO NPs with the gradient content and different topographies, respectively, as shown in Figure 3d. Specific capacitance values are summarized in Table S3. As the activation of ZnO NWs enhances (i.e., its content increases), the specific areal capacitance of ZNWC-MSCs increases correspondingly but decreases significantly at 20 wt %, as shown in the red line of Figure 3d, which also gives the similar variation for ZNPC-MSCs (black line). The highest specific areal capacitance of  $8.83 \text{ mF cm}^{-2}$  is obtained at 15 ZNWC-MSC, which is about 6 times higher than that of C-MSC. The volume capacitance of 15 ZNWC-MSC is  $20.06 \text{ F cm}^{-3}$ . The specific capacitances of ZNWC-MSCs are 1.6–5.0 times higher than those of ZNPC-MSCs, which results in acceptable difference with the change

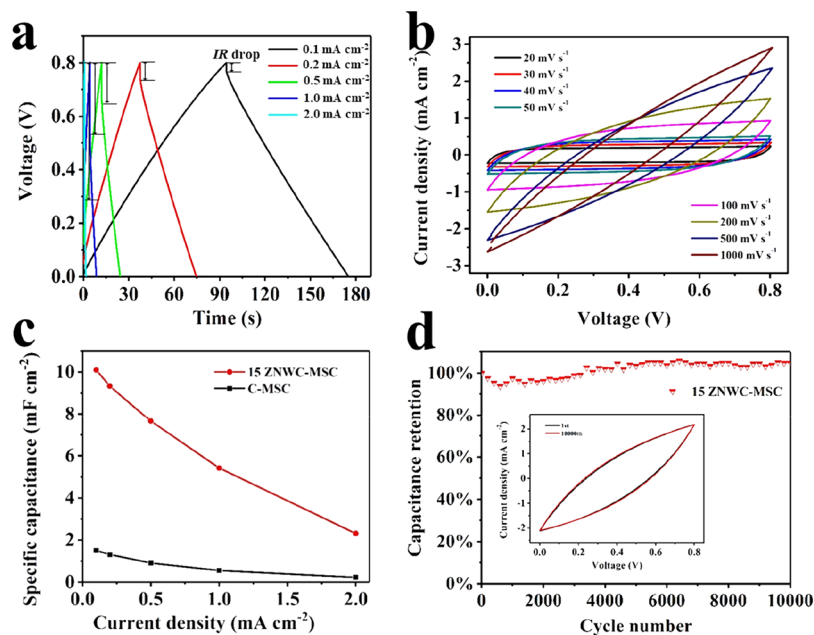


**Figure 5.** Electrochemical performances of 15 ZNWC-MSC. (a) GCD curves at different current densities and (b) CV curves of 15 ZNWC-MSC. (c) Specific capacitances (vs current density) of 15 ZNWC-MSC and C-MSC. (d) Cyclic performance of 15 ZNWC-MSC; the inset shows CV curves at first cycle and 10 000th cycle, respectively.

of amount of ZnO. Thus, two rules are required to be investigated thoroughly or explained clearly by further characterizations. First, universal law confirmed that the specific capacitance based on EDLC and SSA of the electrode has a positive correlation. However, 20 ZNWC-MSC with the highest SSA of  $790.83 \text{ m}^2 \text{ g}^{-1}$  only delivered a specific capacitance of  $4.69 \text{ mF cm}^{-2}$ , much lower than that of 15 ZNWC-MSC. Second, the pyrolyzed carbon activated by low-content ZnO NWs shows a lower SSA and higher specific capacitance than those of pyrolyzed carbon activated by high-content ZnO NPs. We speculate that the channel hierarchical pore structure plays a very important role in improving the specific capacitance of MSCs.

In order to deeply investigate the mechanism of electrochemical performance of ZNWC-MSCs and ZNPC-MSCs, electrochemical impedance spectroscopy (EIS) measurements were performed. Figure 3e exhibits the dynamics process of the electrode, EDLC, and ion diffusion of ZNPC-MSCs. In high frequencies, the Nyquist plots of 5, 10, and 15 ZNPC-MSCs reveal a relatively similar charge-transfer resistance related to the electrical conductivity of the electrode and ion conductivity of the electrolyte (inset of Figure 3e). For 20 ZNPC-MSC, there emerges a sharp decrease of surface charge conductivity in Figure 3e. During the pyrolysis process (i.e., the carbonization of organic matter and the sacrifice of carbon because of the oxidation by ZnO), the changes of SSA per unit volume and the number of carbon atoms per unit SSA (called as the areal atomic ratio, a more detailed mathematical model mentioned in previous reports) cause us great concern because of the difference of calculation of volume and mass of the electrode.<sup>33</sup> The areal atomic ratio (Note 2 in the Supporting Information) plays an important role in charge-transfer resistance of the electrode, as shown in Figure 4a. With the deeper sacrifice of carbon and the increase of SSA of microelectrodes activated by 5–20 wt % ZnO NPs, respectively, the areal atomic ratio of the microelectrode will increase and the electron conduction path per unit SSA of the

microelectrode will decrease sharply, which indicates the existence of the threshold of charge-transfer resistance exhibited in 15 ZNPC-MSC.

In low frequencies, the slope of Nyquist plot reflects the property of ion diffusion related to the pore structure of EDLC. Thus, it is obviously confident that the enhancement of ion diffusion with ZNPC-MSCs from 5 to 15 wt % ZnO NPs, and 20 ZNPC-MSC performed relatively poor ion diffusion. For EDLC, the Nyquist plot in low frequency related to the process of ion diffusion control yields a phase angle of  $\pi/2$ . The impedance of a semi-infinite, right cylindrical pore in perfect conductor could be described as

$$Z_{\text{pore}} = (R|Z|)^{1/2} e^{i\varphi/2}$$

where  $R$  is the resistance per unit length down the pore,  $Z$  is the impedance for interfacial impedance at the (wall) plane surface, and  $\varphi$  is the phase angle for that.<sup>42,45</sup> The variation of ion diffusion with ZNPC-MSCs could be explained concisely after the establishment of relation between the length of pores and roughness. The excess activated pyrolyzed carbon possessed a higher specific pore volume of 4 nm, and sub-2 nm could be construed as the nature of roughness of the interface between the electrode and electrolyte, which illustrates the threshold of slope with the Nyquist plot in low frequency for 15 ZNPC-MSCs. It is indicated that excess activation of pyrolyzed carbon increases its ion diffusion resistance.

Similar to ZNPC-MSCs, the charge-transfer property of ZNWC-MSCs also presented a threshold and decrease in 20 ZNWC-MSC, which is attributed to the increase of the areal atom ratio owing to the activation and sacrifice of glassy carbon. However, the slope of Nyquist plots in high frequency for ZNWC-MSCs remains basically the same, different from the result of ZNPC-MSCs. To further investigate the status of the electrolyte in the thin carbon electrode film activated by 15 wt % ZnO NWs, the EDS line scanning was conducted. It is

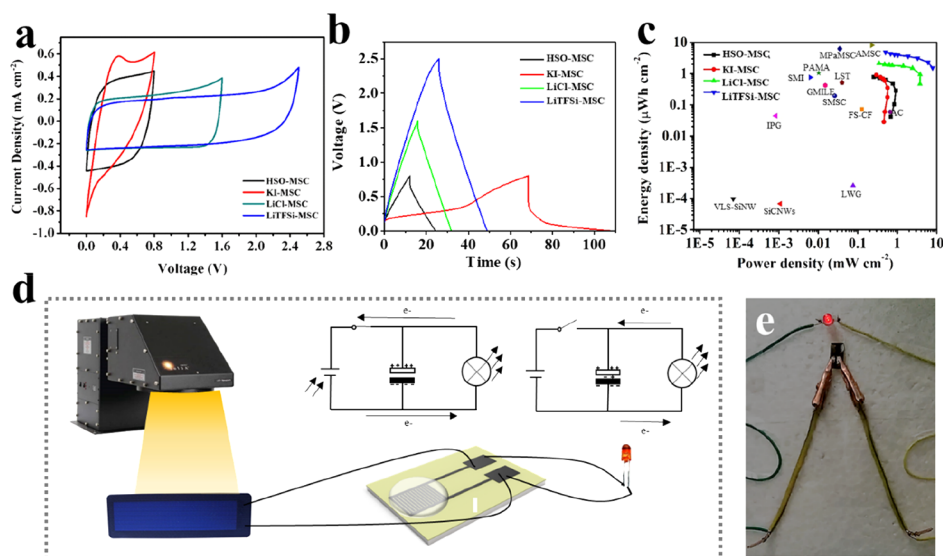


**Figure 6.** Electrochemical performances of 15 ZNWC-MSC with various electrolytes. (a) CV curves, (b) GCD curves, and (c) Ragone plots of different planar MSCs comparing the areal energy density and power density of 15 ZNWC-MSC employing electrolytes of  $\text{H}_2\text{SO}_4$ , KI, LiCl, and LiTFSi with full-inkjet-printing graphene (IPG),  $\text{MnO}_2/\text{PANI}$  asymmetrical (MPaMSC),<sup>10</sup>  $\text{MnO}_2/\text{PPy}$  asymmetrical MSCs (MPMSC),<sup>11</sup>  $\text{MnO}_2$  asymmetrical MSC (SMSC),<sup>11</sup> laser-scribing rGO-coated textile (LST),<sup>18</sup> graphene quantum dots/ $\text{MnO}_2$  with ionic liquid gel electrolytes (GMILE),<sup>25</sup> printing Au/ $\text{MnO}_2$ /Au (PAMA),<sup>32</sup> freestanding carbon films (FS-CF),<sup>2</sup> AC,<sup>37</sup> laser-written graphene (LWG),<sup>38</sup> vapor–liquid–solid grown silicon NWs (VLS-Si Nws),<sup>43</sup> silicon carbide NWs (SiC NWs),<sup>44</sup> and stamping MXene inks.<sup>16</sup> (d) Schematic diagram and circuit diagram of integration of solar cell (energy-harvesting device) and 15 ZNWC-MSC with LiTFSi as the electrolyte (energy storage device). (e) Single 15 ZNWC-MSC with the LiTFSi electrolyte could light up an LED.

confirmed that the electrolyte is infiltrated to the pores (Figure S9). The invalid SSA related to the electrolyte infiltration of pyrolyzed carbon activated by ZnO NPs and ZnO NWs is visualized by white squares in Figure 4b,c. On the basis of the assumption with the similar or same SSA of pyrolyzed carbon activated by ZnO NPs and ZnO NWs, we could confirm that the latter could provide higher EDLC because of the higher efficient utilization of SSA for 3D channel pores and the formation of electrolyte cistern accumulating its Ohmic resistance (Note 2 in the Supporting Information). The pores in the diameter of about 100 nm are performed as the electrolyte cistern without the impact of solvent–ion condition. It increases the electrolyte pathway to access the surface and thus to accelerate ion conduction of the electrolyte-flooded matrix related to the distribution of Ohmic resistance (Figure 4b,c). Also, the previous work identified that the unreasonable micropore structure aggravates the repulsion between counterions affected.<sup>34,46,47</sup> The channel cross-linking macropores further improve ion diffusion related to the mesopores on the wall of template pores and shorten the ion-transfer length relatively. We confirmed that the macropore structure etched by ZnO NWs demonstrates the optimal performance of ion diffusion owing to the coordination of Ohmic accumulation by the electrolyte in the channel pores and ion diffusion in mesopores. The Bode plots of impedance of ZNWC and ZNPC MSCs are shown in Figure S10. The time constant  $\tau$  of 15 ZNWC-MSC is 1.56 s, much lower than those of 10 ZNWC-MSC (2.75 s), 20 ZNWC-MSC (5.34 s), and 15 ZNPC-MSC (3.74 s). It is indicated that the electrochemical performance of MSCs at high scan rate is enhanced by moderate activation (considerable areal atomic ratio) and the interconnected channel pore structure. The microelectrode is different from the microelectrode assembled by carbon particles. The monolithic structure provides a continuous electron pathway. The 3D interconnected porous

structure provides a continuous electrolyte diffusion pathway. Therefore, the bicontinuous pathway of electron conduction and ion diffusion improves the electrochemical reaction kinetic and the performance of the microelectrode.

After clarifying the improvement of specific areal capacitance of ZNPC-MSCs and ZNWC-MSCs (Table S3), we further studied the electrochemical performance of 15 ZNWC-MSC in detail (Figure 5). As shown in Figure 5a, the GCD curves of 15 ZNWC-MSC collected under 0.1–2  $\text{mA cm}^{-2}$  exhibit a symmetric triangular shape corresponding to the EDLC mechanism. The specific areal capacitance of 15 ZNWC-MSC is  $10.01 \text{ mF cm}^{-2}$  calculated from the GCD curve at the current density of  $0.1 \text{ mA cm}^{-2}$ . What is worth noting is the IR drop related to the charge-transfer resistance of ions and electrons. Considering that the pyrolyzed carbon is used as the metal-free self-current collector, the value of IR drop related to the rate performance is acceptable, leading to the rectangle distortion of CV curves at a relatively higher scan rate (Figure 5b). Thus, the rate performances of 15 ZNWC-MSC and C-MSC shown in Figure 5c show that the specific areal capacitance of 15 ZNWC-MSC is always more than five times that of C-MSC. In addition, the cyclic stability of 15 ZNWC-MSC under the scan rate of  $500 \text{ mV s}^{-1}$  exhibits 105% of the capacitance retention after 10 000 cycles (Figure 5d). The increase of capacitance is due to the further infiltration of the electrolyte into the microelectrode. After 4000th cycles, the capacitance of the MSC is stable. The Coulombic efficiency of 15 ZNWC-MSC is almost higher than 99.5% (Figure S12). The original morphology of the interconnected channel pore is maintained after cycling (Figure S13).

The energy density of MSCs is proportional to the specific capacity and the square of working voltage. To increase the energy density of MSCs, we assembled 15 ZNWC-MSCs with  $\text{H}_2\text{SO}_4$  (acidic electrolyte), redox additive KI/ $\text{H}_2\text{SO}_4$ , LiCl (neutral electrolyte), and LiTFSi [ $\text{LiN}(\text{SO}_2\text{CF}_3)_2$ , water-in-salt

electrolyte] electrolytes, which are noted as HSO-MSC, KI-MSC, LiCl-MSC, and LiTFSi-MSC. As shown in Figure 6a, HSO-MSC exhibits the relatively higher response current density, which is mainly due to the coordination in the size of pores and solvated ions. Owing to the redox reaction on the interface of the electrode and KI electrolyte, the CV curve of KI-MSC shows the redox peaks with improved response current density (Figure 6b). After measuring the self-discharge of KI-MSC, we confirm that the feasibility of using KI in MSC needs to be improved because of the drastic self-discharge drawback related to the structure of MSC, such as very short diffusion distance and separation-free device structure (Figure S14). As for the neutral electrolyte with low  $H^+$  or  $OH^-$  concentration, LiCl withstands the voltage window of  $\sim 1.6$  V based on its high stable voltage (Figure S15). The polarization and coordination in the size of pores and ions have an impact on the performance of LiCl-MSC partly, which reduce the specific capacitance ( $5.98 \text{ mF cm}^{-2}$  at the scan rate of  $20 \text{ mV s}^{-1}$ ), respectively. To enhance the stable voltage window with acceptable breakage of performance, water-in-salt electrolyte LiTFSi is employed as the electrolyte, revealing the higher voltage window of 2.5 V (Figure S16). LiTFSi-MSC shows a similar specific capacitance of  $5.62 \text{ mF cm}^{-2}$  at the scan rate of  $20 \text{ mV s}^{-1}$  with LiCl-MSC. The Ragone plot visualizes the value of energy density and power density of MSC with above electrolytes, respectively, which strengthened the great application potential of LiTFSi (Figure 6c). As the first attempt of the redox electrolyte on MSCs, we confirm that KI could improve the specific capacitance, but the urgent problem to be solved is its relatively low reaction potential and high self-discharge rate. Compared with HSO-MSC and KI-MSC, LiCl-MSC delivers the balanced properties including energy density and industrial costs (Figure S17). LiTFSi-MSC delivered the highest area energy density of  $4.9 \mu\text{W h cm}^{-2}$  and volume energy density of  $11.13 \text{ mW h cm}^{-3}$ , which are about 6 times higher than those of HSO-MSC. It also showed the highest power density of  $7.92 \text{ mW cm}^{-2}$  at the energy density of  $1.53 \mu\text{W h cm}^{-2}$ . The energy density and power density of LiTFSi-MSC are also higher than those of previously reported MSCs (Table S4).

Because of its ultrahigh energy density and adaptive voltage, the single LiTFSi-MSC was integrated with the solar cell as the energy-harvesting device to light up an LED (Figure 6d,e). When the solar energy was cut off, the LED was still lit. It is worth noting that the operating voltage of an LED is 1.8–2.2 V. Single MSC with a common aqueous electrolyte whose potential window is usually  $< 1.8$  V cannot drive an LED. The series and parallel connection will increase the complexity of the whole device. Therefore, the single LiTFSi MSC will reduce the cost of integrated devices. It is worth noting that the microliter level of the LiTFSi electrolyte on one piece of MSC will not obviously increase the cost of MSC compared with that of the microfabrication process.

## CONCLUSIONS

In summary, a 3D interconnected bicontinuous porous carbon MSC has been constructed by the controllable activation method. The optimized ZNWC-MSC shows an areal specific capacitance of  $10.01 \text{ mF cm}^{-2}$ , which is 1.6–5 times higher than that of ZNPC-MSC and 6 times higher than that of pure pyrolyzed carbon MSC. The SSA of the composite micro-electrode is increased because of the interconnected porous structure. Four kinds of electrolytes have been studied for

increasing the energy density of MSCs. The energy density of LiTFSi-MSC is 6 times higher than that of HSO-MSC. Because of its ultrahigh energy density and adaptive voltage, the single LiTFSi MSC can be integrated with the solar cell as the energy-harvesting device to light up an LED. The high-performance 3D interconnected porous carbon MSC shows a great potential in applications of large-scale integration of micro-/nanodevices and systems.

## ASSOCIATED CONTENT

### Supporting Information

The Supporting Information is available free of charge on the ACS Publications website at DOI: 10.1021/acsami.8b18853.

Materials synthesis and characterization; electrochemical measurements; SEM images and XRD patterns of ZnO nanomaterials; SEM images and XRD patterns of ZNPC; TG–DSC curves of 15 wt % ZnO NWs/ photoresist; BET results and Raman spectra of ZNPC; CV and GCD curves of ZNPC-MSCs; EDS line scan spectra of 15 ZNWC-MSC after test; rate performance of ZNPC-MSC; CV and GCD curves of KI-MSC/LiCl-MSC/LiTFSi-MSC; rate performance of 15 ZNWC-MSCs with different electrolytes; SSA values of ZNWC and ZNPC; IR drop and specific areal capacitances of ZNWC and ZNPC MSCs; and comparison of various MSCs (PDF)

## AUTHOR INFORMATION

### Corresponding Authors

\*E-mail: hel@whut.edu.cn (L.H.).

\*E-mail: mlq518@whut.edu.cn (L.M.).

### ORCID

Lin Xu: 0000-0003-2347-288X

Xuelei Pan: 0000-0002-8317-2080

Liqiang Mai: 0000-0003-4259-7725

### Author Contributions

X.M. and X.H. make the equal contribution to this work.

### Notes

The authors declare no competing financial interest.

## ACKNOWLEDGMENTS

This work was supported by the National Key Research and Development Program of China (2016YFA0202603 and 2016YFA0202604), the Programme of Introducing Talents of Discipline to Universities (B17034), the National Natural Science Foundation of China (51502227, 51579198, and 51521001), the National Natural Science Fund for Distinguished Young Scholars (51425204), the China Postdoctoral Science Foundation (2015T80845), and the Wuhan Morning Light Plan of Youth Science and Technology (no. 2017050304010316). The State Key Laboratory of Advanced Technology for Materials Synthesis and Processing (WUT: 2018-KF-7, 2018-ZD-1). We thank Prof. Xudong Wang of the University of Wisconsin-Madison for strong support and stimulating discussions.

## REFERENCES

- (1) Li, J.; Deleka, S. S.; Zhang, P.; Yang, S.; Lohe, M. R.; Zhuang, X.; Feng, X.; Östling, M. Scalable Fabrication and Integration of Graphene Microsupercapacitors through Full Inkjet Printing. *ACS Nano* 2017, 11, 8249–8256.

- (2) Huang, P.; Lethien, C.; Pinaud, S.; Brousse, K.; Laloo, R.; Turq, V.; Respaud, M.; Demortiere, A.; Daffos, B.; Taberna, P. L.; Chaudret, B.; Gogotsi, Y.; Simon, P. On-Chip and Freestanding Elastic Carbon Films for Micro-supercapacitors. *Science* **2016**, *351*, 691–695.
- (3) Choudhary, N.; Li, C.; Moore, J.; Nagaiah, N.; Zhai, L.; Jung, Y.; Thomas, J. Asymmetric Supercapacitor Electrodes and Devices. *Adv. Mater.* **2017**, *29*, 1605336.
- (4) Shaijumon, M. M.; Perre, E.; Daffos, B.; Taberna, P.-L.; Tarascon, J.-M.; Simon, P. Nanoarchitected 3D Cathodes for Li-ion Microbatteries. *Adv. Mater.* **2010**, *22*, 4978–4981.
- (5) Mirvakili, S. M.; Hunter, I. W. Vertically Aligned Niobium Nanowire Arrays for Fast-Charging Micro-Supercapacitors. *Adv. Mater.* **2017**, *29*, 1700671.
- (6) Liu, W.; Lu, C.; Wang, X.; Tay, R. Y.; Tay, B. K. High-Performance Microsupercapacitors Based on Two-Dimensional Graphene/Manganese Dioxide/Silver Nanowire Ternary Hybrid Film. *ACS Nano* **2015**, *9*, 1528–1542.
- (7) Anasori, B.; Lukatskaya, M. R.; Gogotsi, Y. 2D Metal Carbides and Nitrides (MXenes) for Energy Storage. *Nat. Rev. Mater.* **2017**, *2*, 16098.
- (8) Xiong, T.; Tan, T. L.; Lu, L.; Lee, W. S. V.; Xue, J. Harmonizing Energy and Power Density toward 2.7 V Asymmetric Aqueous Supercapacitor. *Adv. Energy Mater.* **2018**, *8*, 1702630.
- (9) Kyeremateng, N. A.; Brousse, T.; Pech, D. Microsupercapacitors as Miniaturized Energy-Storage Components for On-Chip Electronics. *Nat. Nanotechnol.* **2017**, *12*, 7–15.
- (10) Wang, X.; Sumboja, A.; Foo, W. L.; Yan, C. Y.; Tsukagoshi, K.; Lee, P. S. Rational Design of a High Performance All Solid State Flexible Micro-Supercapacitor on Paper. *RSC Adv.* **2013**, *3*, 15827–15833.
- (11) Guo, R.; Chen, J.; Yang, B.; Liu, L.; Su, L.; Shen, B.; Yan, X. In-Plane Micro-Supercapacitors for an Integrated Device on One Piece of Paper. *Adv. Funct. Mater.* **2017**, *27*, 1702394.
- (12) Ma, X.; Feng, S.; He, L.; Yan, M.; Tian, X.; Li, Y.; Tang, C.; Hong, X.; Mai, L. Rapid, All Dry Microfabrication of Three-Dimensional Co<sub>3</sub>O<sub>4</sub>/Pt Nanonetworks for High-performance Micro-supercapacitors. *Nanoscale* **2017**, *9*, 11765–11772.
- (13) Tian, X.; Shi, M.; Xu, X.; Yan, M.; Xu, L.; Minhas-Khan, A.; Han, C.; He, L.; Mai, L. Arbitrary Shape Engineerable Spiral Micropseudocapacitors with Ultrahigh Energy and Power Densities. *Adv. Mater.* **2015**, *27*, 7476–7482.
- (14) Liu, Z.; Tian, X.; Xu, X.; He, L.; Yan, M.; Han, C.; Li, Y.; Yang, W.; Mai, L. Capacitance and Voltage Matching Between MnO<sub>2</sub> Nanoflake Cathode and Fe<sub>2</sub>O<sub>3</sub> Nanoparticle Anode for High-Performance Asymmetric Micro-Supercapacitors. *Nano Res.* **2017**, *10*, 2471–2481.
- (15) Xiao, H.; Wu, Z.-S.; Chen, L.; Zhou, F.; Zheng, S.; Ren, W.; Cheng, H.-M.; Bao, X. One-Step Device Fabrication of Phosphorene and Graphene Interdigital Micro-Supercapacitors with High Energy Density. *ACS Nano* **2017**, *11*, 7284–7292.
- (16) Zhang, C. J.; Kremer, M. P.; Seral-Ascaso, A.; Park, S.-H.; McEvoy, N.; Anasori, B.; Gogotsi, Y.; Nicolosi, V. Stamping of Flexible, Coplanar Micro-Supercapacitors Using MXene Inks. *Adv. Funct. Mater.* **2018**, *28*, 1705506.
- (17) Wang, X.; Wan, F.; Zhang, L.; Zhao, Z.; Niu, Z.; Chen, J. Large-Area Reduced Graphene Oxide Composite Films for Flexible Asymmetric Sandwich and Microsized Supercapacitors. *Adv. Funct. Mater.* **2018**, *28*, 1707247.
- (18) Pu, X.; Liu, M.; Li, L.; Han, S.; Li, X.; Jiang, C.; Du, C.; Luo, J.; Hu, W.; Wang, Z. L. Wearable Textile-Based In-Plane Micro-supercapacitors. *Adv. Energy Mater.* **2016**, *6*, 1601254.
- (19) Simon, P.; Gogotsi, Y. Materials for Electrochemical Capacitors. *Nat. Mater.* **2008**, *7*, 845.
- (20) Li, X.; Wei, J.; Li, Q.; Zheng, S.; Xu, Y.; Du, P.; Chen, C.; Zhao, J.; Xue, H.; Xu, Q.; Pang, H. Nitrogen-Doped Cobalt Oxide Nanostructures Derived from Cobalt-Alanine Complexes for High-Performance Oxygen Evolution Reactions. *Adv. Funct. Mater.* **2018**, *28*, 1800886.
- (21) Li, B.; Gu, P.; Feng, Y.; Zhang, G.; Huang, K.; Xue, H.; Pang, H. Ultrathin Nickel-Cobalt Phosphate 2D Nanosheets for Electrochemical Energy Storage under Aqueous/Solid-State Electrolyte. *Adv. Funct. Mater.* **2017**, *27*, 1605784.
- (22) Lam, D. V.; Jo, K.; Kim, C.-H.; Kim, J.-H.; Lee, H.-J.; Lee, S.-M. Activated Carbon Textile via Chemistry of Metal Extraction for Supercapacitors. *ACS Nano* **2016**, *10*, 11351–11359.
- (23) Yu, S.; Wang, H.; Hu, C.; Zhu, Q.; Qiao, N.; Xu, B. Facile Synthesis of Nitrogen-Doped, Hierarchical Porous Carbons with a High Surface Area: the Activation Effect of a nano-ZnO Template. *J. Mater. Chem. A* **2016**, *4*, 16341–16348.
- (24) Li, X.; Zheng, S.; Jin, L.; Li, Y.; Geng, P.; Xue, H.; Pang, H.; Xu, Q. Metal-Organic Framework-Derived Carbons for Battery Applications. *Adv. Energy Mater.* **2018**, *8*, 1800716.
- (25) Shen, B.; Lang, J.; Guo, R.; Zhang, X.; Yan, X. Engineering the Electrochemical Capacitive Properties of Microsupercapacitors Based on Graphene Quantum Dots/MnO<sub>2</sub> Using Ionic Liquid Gel Electrolytes. *ACS Appl. Mater. Interfaces* **2015**, *7*, 25378–25389.
- (26) Lee, K.; Lee, H.; Shin, Y.; Yoon, Y.; Kim, D.; Lee, H. Highly Transparent and Flexible Supercapacitors Using Graphene-Graphene Quantum Dots Chelate. *Nano Energy* **2016**, *26*, 746–754.
- (27) Wang, G.; Zhang, L.; Zhang, J. A Review of Electrode Materials for Electrochemical Supercapacitors. *Chem. Soc. Rev.* **2012**, *41*, 797–828.
- (28) Jiang, H.; Lee, P. S.; Li, C. 3D Carbon based Nanostructures for Advanced Supercapacitors. *Energy Environ. Sci.* **2013**, *6*, 41–53.
- (29) Beidaghi, M.; Wang, C. Micro-Supercapacitors Based on Three Dimensional Interdigital Polypyrrole/C-MEMS Electrodes. *Electrochim. Acta* **2011**, *56*, 9508–9514.
- (30) Toupin, M.; Brousse, T.; Bélanger, D. Charge Storage Mechanism of MnO<sub>2</sub> Electrode Used in Aqueous Electrochemical Capacitor. *Chem. Mater.* **2004**, *16*, 3184–3190.
- (31) Zhang, J.; Chen, P.; Oh, B. H. L.; Chan-Park, M. B. High Capacitive Performance of Flexible and Binder-Free Graphene-Polypyrrole Composite Membrane based on In Situ Reduction of Graphene Oxide and Self-Assembly. *Nanoscale* **2013**, *5*, 9860–9866.
- (32) Hu, H.; Pei, Z.; Fan, H.; Ye, C. 3D Interdigital Au/MnO<sub>2</sub>/Au Stacked Hybrid Electrodes for On-Chip Microsupercapacitors. *Small* **2016**, *12*, 3059–3069.
- (33) Simon, P.; Gogotsi, Y.; Dunn, B. Where Do Batteries End and Supercapacitors Begin? *Science* **2014**, *343*, 1210–1211.
- (34) Prehal, C.; Koczwar, C.; Jäckel, N.; Schreiber, A.; Burian, M.; Amenitsch, H.; Hartmann, M. A.; Presser, V.; Paris, O. Quantification of Ion Confinement and Desolvation in Nanoporous Carbon Supercapacitors with Modelling and In Situ X-ray Scattering. *Nat. Energy* **2017**, *2*, 16215.
- (35) Zhang, W.; Xu, C.; Ma, C.; Li, G.; Wang, Y.; Zhang, K.; Li, F.; Liu, C.; Cheng, H.-M.; Du, Y.; Tang, N.; Ren, W. Nitrogen-Superdoped 3D Graphene Networks for High-Performance Supercapacitors. *Adv. Mater.* **2017**, *29*, 1701677.
- (36) Conway, B. E. *Electrochemical Supercapacitors: Scientific Fundamentals and Technological Applications*; Plenum Press, 1999; p 21.
- (37) Pech, D.; Brunet, M.; Durou, H.; Huang, P.; Mochalin, V.; Gogotsi, Y.; Taberna, P.-L.; Simon, P. Ultrahigh-Power Micrometre-Sized Supercapacitors based on Onion-like Carbon. *Nat. Nanotechnol.* **2010**, *5*, 651–654.
- (38) Gao, W.; Singh, N.; Song, L.; Liu, Z.; Reddy, A. L. M.; Ci, L.; Vajtai, R.; Zhang, Q.; Wei, B.; Ajayan, P. M. Direct Laser Writing of Micro-Supercapacitors on Hydrated Graphite Oxide Films. *Nat. Nanotechnol.* **2011**, *6*, 496–500.
- (39) Hsia, B.; Kim, M. S.; Vincent, M.; Carraro, C.; Maboudian, R. Photoresist-Derived Porous Carbon for On-Chip Micro-Supercapacitors. *Carbon* **2013**, *57*, 395–400.
- (40) Yang, Y.; He, L.; Tang, C.; Hu, P.; Hong, X.; Yan, M.; Dong, Y.; Tian, X.; Wei, Q.; Mai, L. Improved Conductivity and Capacitance of Interdigital Carbon Microelectrodes through Integration with Carbon Nanotubes for Micro-supercapacitors. *Nano Res.* **2016**, *9*, 2510–2519.

(41) Hong, X.; He, L.; Ma, X.; Yang, W.; Chen, Y.; Zhang, L.; Yan, H.; Li, Z.; Mai, L. Microstructuring of Carbon/Tin Quantum Dots via a Novel Photolithography and Pyrolysis-Reduction Process. *Nano Res.* **2017**, *10*, 3743–3753.

(42) Yang, W.; He, L.; Tian, X.; Yan, M.; Yuan, H.; Liao, X.; Meng, J.; Hao, Z.; Mai, L. Carbon-MEMS-Based Alternating Stacked MoS<sub>2</sub>@rGO-CNT Micro-Supercapacitor with High Capacitance and Energy Density. *Small* **2017**, *13*, 1700639.

(43) Thissandier, F.; Le Comte, A.; Crosnier, O.; Gentile, P.; Bidan, G.; Hadji, E.; Brousse, T.; Sadki, S. Highly Doped Silicon Nanowires based Electrodes for Micro-Electrochemical Capacitor Applications. *Electrochem. Commun.* **2012**, *25*, 109–111.

(44) Alper, J. P.; Kim, M. S.; Vincent, M.; Hsia, B.; Radmilovic, V.; Carraro, C.; Maboudian, R. Silicon Carbide Nanowires as Highly Robust Electrodes for Micro-Supercapacitors. *J. Power Sources* **2013**, *230*, 298–302.

(45) Macdonald, D. D. Reflections on the History of Electrochemical Impedance Spectroscopy. *Electrochim. Acta* **2006**, *51*, 1376–1388.

(46) Rose, M.; Korenblit, Y.; Kockrick, E.; Borchardt, L.; Oschatz, M.; Kaskel, S.; Yushin, G. Hierarchical Micro- and Mesoporous Carbide-Derived Carbon as a High-Performance Electrode Material in Supercapacitors. *Small* **2011**, *7*, 1108–1117.

(47) Merlet, C.; Rotenberg, B.; Madden, P. A.; Taberna, P.-L.; Simon, P.; Gogotsi, Y.; Salanne, M. On the Molecular Origin of Supercapacitance in Nanoporous Carbon Electrodes. *Nat. Mater.* **2012**, *11*, 306–310.